

Insight into the in-situ surface reconstruction of perovskite BiFeO₃ for boosting nitrate electroreduction to ammonia

Lihui Yang^{a,1,*}, Wenjian Yang^{a,1}, Shangtao Liang^b, Zeqin Lin^a, Jianxin Pan^a, Cao Yang^a, Tingting Zhu^c, Sihao Lv^a, Hui Lin^{a,*}

^a Research Center for Eco-environmental Engineering, Dongguan University of Technology, Dongguan 523808, PR China

^b College of Agricultural and Environmental Sciences, Department of Crop and Soil Sciences, University of Georgia, Griffin, GA 30223, United States

^c School of Environmental Science and Engineering, Tianjin University, Tianjin 300072, PR China

ARTICLE INFO

Keywords:

Perovskite BiFeO₃
Surface reconstruction
Nitrate electroreduction
Metallic Bi⁰ clusters

ABSTRACT

Nitrate electroreduction (NO₃RR) is a promising alternative route for green synthesis of ammonia, where high-efficient catalysts are desired. Herein, an inexpensive ABO₃-type perovskite BiFeO₃ was demonstrated as a highly efficient NO₃RR catalyst compared to most of the reported non-precious catalysts. More interestingly, a surface evolution is observed in conjunction with an enhancement in NH₃ yield rate during the NO₃RR process. Numerous metallic Bi⁰ clusters and oxygen vacancies (OVs) are in-situ generated in the reconstructed BiFeO₃ (RS-BiFeO₃), and are proposed to be the genuine active sites. Density functional theory calculations suggest the RS-BiFeO₃ promotes the conversion of *NO₂ to *NO and enhances the *H supply for NO₃ hydrogenation, thus boosting NO₃RR. The yield rate of NH₃ by the reconstructed BiFeO₃ electrode reaches 5.3 mg cm⁻² h⁻¹ with a Faradaic efficiency of 86.8% at -0.7 V vs. RHE, over 4 times higher than that of the pristine BiFeO₃ electrode. This study establishes a fundamental understanding of BiFeO₃ reconstruction during NO₃RR, and provides insights for the rational design of perovskite NO₃RR electrocatalysts.

1. Introduction

Ammonia (NH₃) is a fundamental chemical feedstock with widespread use in agriculture and industrial manufacture, and it also serves as a promising carbon-free energy carrier in direct ammonia fuel cells and hydrogen generation [1,2]. Currently, the Haber-Bosch process is the predominant method for industrial NH₃ production, but it is associated with high energy consumption and substantial CO₂ emissions. Recently, electrochemical NH₃ synthesis, especially, NO₃ electroreduction reaction (NO₃RR), conducted at room temperature and ambient pressure and powered by renewable energy, has garnered considerable interest as a sustainable method for green ammonia production [3,4]. Nonetheless, due to the complex eight-electron reduction involved in NO₃RR process and the competing hydrogen evolution reaction (HER), this method typically results in low activity and poor selectivity [5,6]. Therefore, developing efficient NO₃RR electrocatalysts remains a great challenge.

Unveiling the true active sites of NO₃RR catalysts under reaction

conditions is crucial for the rational design of efficient electrocatalysts, given that structural evolution may occur under potential-driven conditions during the electroreduction process [7–9]. Furthermore, the reconstruction process can modulate electrocatalytic behaviors, such as adsorption, activation, and desorption, during electroreduction reaction, thereby influencing catalytic activity [10–12]. For instance, Wang et al. reported that a significant activity enhancement for CuO towards NO₃RR originated from the in-situ formed Cu/Cu₂O active phase during the NO₃RR process. They found that the electron transfer from Cu₂O to Cu at the interface could facilitate the formation of *NOH intermediate and suppress the HER process, leading to high NH₃ selectivity of 81.20% and a Faradaic efficiency of 95.80% [11]. Another study reported that Cu₅Ru₁O_x was reconstructed to Ru&Cu/Cu₂O after electroreduction, which resulted in significantly enhanced adsorption of NO₃ and a more favorable proton supply for NO₃ hydrogenation. This change led to a 1.2-fold increase in Faradaic efficiency and a 1.4-fold increase in NH₃ selectivity, respectively [12]. Therefore, unveiling the structure-activity relationship's intricacies is vital for guiding the design of dedicated

* Corresponding authors.

E-mail addresses: yanglh@dgut.edu.cn (L. Yang), linhui@dgut.edu.cn (H. Lin).

¹ Lihui Yang and Wenjian Yang contributed equally to this work.

NO₃RR electrocatalysts.

The phenomenon of surface reconstruction is prevalent in transition metal-based electrocatalysts, as their redox potentials often overlap with the working potentials to a certain extent [13,14]. Moreover, a special structure (e.g., oxygen vacancies, OVs) in electrocatalysts tends to more readily trigger reconstruction [15,16]. For instance, the accelerated surface reconstruction of Ni_{1.5}Sn@triMPO₄ was attributed to the presence of OVs, which decrease the vacancy formation energy of Sn atoms and increase the adsorption energy of phosphate anions at O-vacancy sites [16]. Recently, ABO₃-type perovskite oxides, such as LaFeO₃, LaCoO₃, etc [17–19], characterized by flexible electronic structures and chemical versatility, have garnered much attention in NO₃RR. Specifically, bismuth ferrite (BiFeO₃), was reported to exhibit exceptional NO₃RR catalytic activity, achieving a Faradaic efficiency of 96.85% and a NH₃ yield rate of 90.45 mg mg_{cat}⁻¹h⁻¹ [20]. As a transition metal-based electrocatalyst that is inherently rich in OVs, the structure of BiFeO₃ might evolve during the NO₃RR process, thereby influencing its catalytic activity. Although Wang et. al., and other researchers have discovered that new phases (e.g., Bi⁰, Bi₂O₃) were generated when BiFeO₃ was used for energy storage and water splitting [21,22], there is limited information regarding how BiFeO₃ restructured during the NO₃RR process and the impact of such changes on its catalytic activity.

In this study, we examine the in-situ surface reconstruction of BiFeO₃ during electrolysis and its impact on the efficiency of NO₃ electroreduction. An enhancement in activity for NO₃-N to NH₃ was observed in tandem with the structural evolution of BiFeO₃, where new phases, especially metallic Bi⁰ cluster and oxygen vacancies (OVs), were in-situ generated. Density functional theory (DFT) was applied to gain insights into the active sites within the reconstructed BiFeO₃ (RS-BiFeO₃) that contribute to the enhanced NO₃RR activity. In situ differential electrochemical mass spectrometry (DEMS) and free radical capture test (e.g., EPR) were performed to analyze the NO₃ electroreduction pathway, further affirming the pivotal role of the active sites of Bi⁰ clusters and OVs. This work provides a comprehensive understanding of surface reconstruction for high-efficiency of NO₃RR on perovskite BiFeO₃ catalysts.

2. Materials and methods

2.1. Chemicals and materials

Bismuth nitrate pentahydrate (Bi(NO₃)₃·5 H₂O, 99.0%), iron nitrate nonahydrate (Fe(NO₃)₃·9 H₂O, 99.9%), citric acid monohydrate (C₆H₈O₇·H₂O, CM, 99.5%), ethylene glycol (C₂H₄O₂, EG, 98.0%), sodium nitrate (NaNO₃, ≥99%), potassium sodium nitrate (K¹⁵NO₃, 99.0%), sodium sulfate (Na₂SO₄, 99.99%), tert-butyl alcohol (TBA, 99.5%), nitric acid (HNO₃, 99.0%), sulfuric acid (H₂SO₄, 99.9%) and 5,5-dimethyl-1-pyrroline-N-oxide (C₅H₆O, DMPO, 97.0) were purchased from Aladdin Co., Ltd. (China). The 5 wt% Nafion solution was procured from Dupont Co., Ltd. (USA). Carbon cloth (WOS1011), used as the electrode substrate, was purchased from Taiwan CeTech Co., Ltd (China). The deionized water (DIW) was utilized throughout the experiments.

2.2. Catalyst synthesis and characterization

The perovskite oxide BiFeO₃ powder was synthesized via a simple sol-gel method. Specifically, nitrate metal cations (Bi(NO₃)₃·5 H₂O, Fe(NO₃)₃·9 H₂O), a chelating agent (CM) and polycondensation agent (EG) were combined with a molar ratio of 1:2:4. The resulting solution was then maintained at 80 °C for 12 hours and subsequently at 120 °C for 10 hours in an oven to form a gel. Following this, the gels underwent heat treatment at 300 °C for 2 hours and were calcined at 700 °C. The process ultimately yielded the yellow BiFeO₃ powder. The catalytic cathode was prepared by applying the BiFeO₃ powder to carbon cloth. The carbon cloth (20*20 mm²) underwent a preliminary acid wash

treatment. Subsequently, 20 mg of BFO powder was mixed with 0.1 mL of Nafion and 1.9 mL of ethanol, and sonicated for 30 min to create an ink. Finally, the ink was applied to the carbon cloth, with an average loading of 5 mg cm⁻².

The phase structures of catalyst were analyzed using an X-ray diffractometer (XRD, XPert Powder, Netherlands) with a Cu-Kα radiation scanning rate of 2° min⁻¹. The morphology of catalyst was observed through a field-emission scanning electron microscope (FE-SEM, Regulus 8100, Japan), while transmission electron microscopy (TEM), high-resolution (HR) TEM and elemental mapping (EDS) were collected using a FEI Talos-F200S (USA) machine. The surface chemistry of the catalysts was further characterized through X-ray photoelectron spectroscopy spectra (XPS, ESCALAB 250Xi, U.S.) with a monochromatic Al Kα source. The Electron Paramagnetic Resonance (EPR) analysis was performed to evaluate radical species and oxygen vacancies using a Bruker A200 spectrometer. The iodometry analysis was performed as an additional method for investigating the content of oxygen vacancies, with details provided in Text S1.

2.3. Nitrate electroreduction experiment

A sealed, divided reactor partitioned by a cation exchange membrane (Ultrix CMI-7000, Membranes International, U.S.) was utilized for NO₃RR. BiFeO₃/CC cathodes, a saturated Ag/AgCl electrode, and a platinum electrode were used as the working, reference and counter electrode, respectively. The electrolyte contained 50 mM Na₂SO₄ (50 mL) with 10 mM of NaNO₃ added to the catholyte as target compound. The influence of different potentials on NO₃-N electroreduction performance was assessed by setting the requisite potentials using a CHI 660E electrochemical workstation. For stability evaluation, the working cathode BiFeO₃/CC remained unchanged for a continuous experiment lasting ~400 h at a constant current density of 15 mA/cm². The details of the experimental device for the stability experiment were shown in Fig. S1.

2.4. Analysis methods

The concentration of NO₃-N was evaluated by ion chromatography (ICS 5000+ AQF-2100 H) using an AS11 analytical column. The concentration of NH₄⁺-N and NO₂-N was determined using a UV-visible spectrophotometer (L5S, Shanghai, China) according to the standard colorimetric method [23]. To ensure the accuracy of the test data, a combination of ion chromatography and the UV-vis method was employed for mutual verification. This information has been provided in Text S2 and illustrated in Fig. S2 in the Supporting Information.

Electrochemical tests, including cyclic voltammetry (CV), linear sweep voltammetry (LSV), and electrochemical impedance spectroscopy (EIS), were performed on an Auto-Lab M204 electrochemical workstation (Metrohm, Netherlands), with a three-electrode configuration.

In situ differential electrochemical mass spectrometry (DEMS) test was carried out using a differential electrochemical mass spectrometer (QAS 100, Linglu Instruments Co. Ltd., China). The electrolyte consists of 0.5 mol/L NaSO₄ and 0.1 M NO₃. Prior to and throughout the testing process, Ar gas was continuously bubbled into the electrolyte. Mass signals were obtained during the LSV test from 0 to -1.6 V vs. SCE at a scan rate of 10 mV s⁻¹. The next cycle commenced after the mass signal returned to baseline, repeating the same condition to minimize accidental errors. The measurement was concluded after four cycles.

The EPR analysis of radical species was conducted using a Bruker A200 spectrometer with DMPO as a spin-trapping agent. The testing parameters were: microwave power = 20.816 mW, microwave frequency = 9.842 GHz; center field = 3505 G, sweep width = 80 G; modulation frequency = 100 kHz, modulation amplitude = 0.8 G. For the EPR analysis of oxygen vacancies, the conditions were as follows: microwave power = 1.78 mW, microwave frequency = 9.850 GHz; center field = 3500.0 G, sweep width = 6000.0 G; modulation frequency

= 100 kHz, modulation amplitude = 1.0 G.

Theoretical simulation calculations were performed within the framework of density functional theory (DFT), as implemented by the Vienna ab initio Simulation Package (VASP) in version 5.4.1. The electronic exchange-correlation interaction was captured by the Perdew-Burke-Ernzerhof (PBE) functional under the generalized gradient approximation. Concurrently, the DFT-D3 method [24] was adopted to account for the weak van der Waals interaction. A plane-wave basis was employed with an electronic cutoff energy set to 500 eV. The convergence thresholds for force and energy during geometry optimization corresponded to 0.02 eV/Å and 10^{-5} eV, respectively. The Brillouin zone was sampled using a Gamma-centered Monkhorst-Pack [25] K-point $5 \times 5 \times 1$ mesh. Additionally, the lattice constant along the z-direction exceeded 15 Å, effectively eliminating the potential for coupling between neighboring images.

2.5. Data calculations

The yield rate of byproducts, e.g., Y_{NH_3} ($\text{mg cm}^{-2} \text{ h}^{-1}$), was calculated using Eq. 1:

$$Y_{\text{NH}_3} = (C_{\text{NH}_3-\text{N}_t} - C_{\text{NH}_3-\text{N}_0}) \times V / (S \times T) / 1000 \quad (1)$$

where $C_{\text{NH}_3-\text{N}_t}$ and $C_{\text{NH}_3-\text{N}_0}$ is the concentration of NH_3 -N at reaction time t and 0 min, respectively, (mg/L), V is the volume of solution (0.05 L), S is the cathode area (4.0 cm^2), T is the total reaction time (3 h). The Faradic efficiency of FE_{NH_3} , η (%), was calculated using Eqs. 2–4.

$$Q_{\text{NH}_3} = 8 \times (C_{\text{NH}_3-\text{N}_t} \times V / M_{\text{N}}) \times F \quad (2)$$

$$Q_t = I \times t \quad (3)$$

$$\eta = Q_{\text{NH}_3-\text{N}_t} / Q_t \times 100\% \quad (4)$$

where M_{N} is the molar mass of N (14 g/mol), F is the Faraday's constant (96485 C/mol^{-1}), I (A) is the applied/generated current. The NO_3^- -N removal rate, $r_{(\text{NO}_3^--\text{N})}$ and NO_2^- -N generation rate, $g_{(\text{NO}_2^--\text{N})}$ was calculated as following Eqs. 5, 6

$$r_{\text{NO}_3^--\text{N}} = (C_{\text{NO}_3^--\text{N}_0} - C_{\text{NO}_3^--\text{N}_t}) \times V / (S \times T) / 1000 \quad (5)$$

$$g_{\text{NO}_2^--\text{N}} = (C_{\text{NO}_2^--\text{N}_t} - C_{\text{NO}_2^--\text{N}_0}) \times V / (S \times T) / 1000 \quad (6)$$

where $C_{\text{NO}_3^-}$ and $C_{\text{NO}_2^-}$ is the concentration of NO_3^- -N at reaction time t and 0 min, respectively, (mg/L), $C_{\text{NO}_2^-}$ and $C_{\text{NO}_3^-}$ is the concentration of NO_2^- -N at reaction time t and 0 min, respectively, (mg/L). The NO_3^- -N removal satisfied the pseudo first order dynamics [26], calculated using Eq. 7:

$$\ln(C_{\text{NO}_3^--\text{N}_t} / C_{\text{NO}_3^--\text{N}_0}) = -kt \quad (7)$$

where k is the rate constant (min^{-1}), t is the reaction time (120 min). The ECSA was estimated according to the formula $\text{ECSA} = C_{\text{dl}}/C_s$, where C_{dl} is the double layer capacitance and is equal to twice of the slope of the double-layer charging current versus the scan rate plot. C_s (general specific capacitance of metal oxide) corresponds to the average double layer capacitance of a smooth oxide surface of approximately $60 \mu\text{F} \cdot \text{cm}^{-2}$ [27].

3. Results and discussion

3.1. NO_3RR efficiency versus reaction-time

The perovskite BiFeO_3 powder was successfully synthesized via sol-gel method, as confirmed by the X-ray diffraction (XRD) patterns, which exhibited a pure hexagonal crystal structure and a space group of $R3c$ (JCPDS no. 82–1254), while no extra diffraction peaks observed

(Fig. S3). Then 20 mg of the as-prepared BiFeO_3 was loaded onto a carbon cloth ($2 \times 2 \text{ cm}$) as the catalytic cathode for NO_3^- electroreduction in a gas-tied H-cell, with an electrolyte composed of 50 mM Na_2SO_4 containing 10 mM NaNO_3 . As Fig. 1a illustrates, the concentration of 10 mM NO_3^- decreased to $0.97 \pm 0.2 \text{ mM}$ after 180 min electrolysis, with the generation of $6.30 \pm 0.31 \text{ mM}$ NH_3 . The substantial accumulation of ammonia suggests that BiFeO_3 could serve as an efficient electrocatalyst for selectively reducing NO_3^- to NH_3 . The behavior of the BiFeO_3 catalyst for NO_3RR efficiency was further assessed over a continuous 15 cycles, with each run lasted for one hour. Intriguingly, both the Faradaic efficiency (FE) and selectivity (S_{NH_3}) of NH_3 were significantly improved in the initial eight cycles then plateaued in the subsequent seven cycles (Fig. 1b). Specifically, the FE and S_{NH_3} were 44.65% and 53.30% in the first cycle, respectively, and increased steadily to 73.20% and 83.10% in the eighth cycle. This phenomenon suggests that the active sites for NO_3RR have evolved, likely due to the restructuring of the BiFeO_3 surface under potential-driven, thus, the surface reconstruction on BiFeO_3 enhanced NO_3RR catalytic activity in the initial eight cycles.

To further confirm the positive impact of surface reconstruction on NO_3RR activity, a series of electrochemical tests were conducted by pristine BiFeO_3 (PR- BiFeO_3) and reconstructed BiFeO_3 (RS- BiFeO_3) electrodes. Here, RS- BiFeO_3 refers to PR- BiFeO_3 that underwent a 10-hour cathodic polarization treatment in a 0.1 M Na_2SO_4 solution at -0.5 V vs. RHE. The linear sweep voltammetry (LSV) spectra in a 100 mM Na_2SO_4 solution with 100 mM NO_3^- were displayed in Fig. 2a. The RS- BiFeO_3 recorded a higher current density compared to PR- BiFeO_3 , indicating superior NO_3RR activity of the RS- BiFeO_3 electrode. Moreover, the enhanced activity of the RS- BiFeO_3 was further reflected in a significantly higher ammonia yield rate and current density (Fig. 2b and Fig. S4) under the testing potentials of -0.7 to -0.3 V vs. RHE. As shown in Fig. 2b, the NH_3 yield rate on RS- BiFeO_3 electrode was 4.1–7.8-folds than that of PR- BiFeO_3 across the entire potential range of -0.7 to -0.3 V vs. RHE. Specifically, NH_3 yield rate by the RS- BiFeO_3 electrode was $5.3 \text{ mg cm}^{-2} \text{ h}^{-1}$ at -0.7 V vs. RHE in 100 mM KOH with 100 mM NO_3^- solution, approximately 4.1 times higher than that of the PR- BiFeO_3 electrode ($1.3 \text{ mg cm}^{-2} \text{ h}^{-1}$). Faraday efficiency of the PR- BiFeO_3 electrode decreases significantly as the electrode potential becomes negative, however, only a slightly lower FE value for the RS- BiFeO_3 electrode was observed at higher potentials (Fig. S5). For example, the FE values were 86.8% and 60.1% at -0.7 V vs. RHE, respectively, for the RS- BiFeO_3 and PR- BiFeO_3 electrodes. In summary, a significantly improved NO_3RR catalytic activity on the RS- BiFeO_3 was confirmed. Moreover, compared with other recently reported non-precious catalysts [1, 28–35] (Fig. 2c, Table S1), RS- BiFeO_3 exhibited excellent performance in terms of NH_3 yield rate and FE, underscoring the efficiency of the RS- BiFeO_3 catalyst. In addition, nitrate-free and 15 N isotope labelling experiments were performed as control experiments to validate the origin of the NH_3 . Preliminary deductions from Fig. 2d suggest that NH_3 originated from NO_3^- in the electrolyte. Furthermore, a ^{15}N isotopic labeling ^1H NMR experiment was conducted (Fig. 2e). The presence of typical $^{15}\text{NH}_3$ peak with doublet peaks effectively exclude NH_3 contamination and confirm that NH_3 is indeed synthesized through the NO_3RR process [36].

A Tafel slope value, determined in a 100 mM Na_2SO_4 solution with 100 mM NO_3^- was 37.6 mV dec^{-1} on RS- BiFeO_3 , substantially lower than that of PR- BiFeO_3 (48.8 mV dec^{-1} ; Fig. 2d), illustrating the enhanced intrinsic catalytic activity of RS- BiFeO_3 electrode. The electrochemically active surface area (ECSA) were calculated using the electrochemical double-layer capacitance (C_{dl}) method [27]. As shown in Fig. 2e, the ECSA of RS- BiFeO_3 was 7.3 mF cm^{-2} , approximately 1.4 times higher than that of PR- BiFeO_3 (5.3 mF cm^{-2}), indicating the creation of new reactive sites on the RS- BiFeO_3 electrode. The RS- BiFeO_3 electrode also exhibited a smaller circular arc (Fig. 3f), which corresponded to a smaller charge transfer resistance (R_{ct}) and faster electron transfer. The R_{ct} fitting values from the Nyquist plots of the RS- BiFeO_3 and PR- BiFeO_3 electrodes were approximately 10Ω and 30Ω , respectively. Therefore,

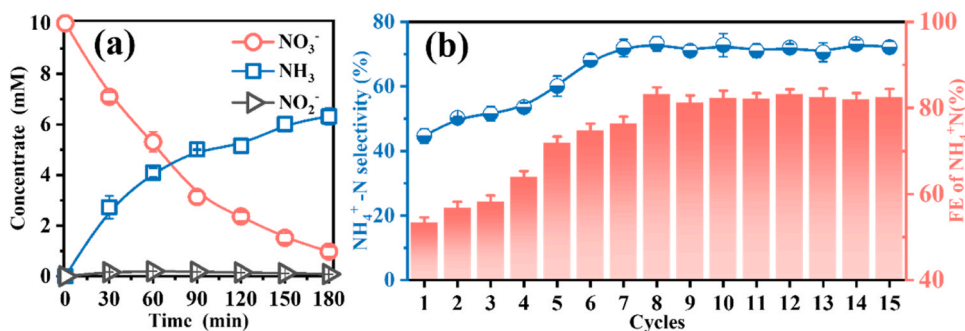


Fig. 1. (a) Time-dependent concentration change of nitrogenous species over RS-BiFeO₃ at -0.5 V vs. RHE with 10 mM of NO₃. (b) Behavior measurements of BiFeO₃ for NO₃ electroreduction. Test conditions: -0.5 V vs. RHE with 10 mM NO₃ for 15 cycles.

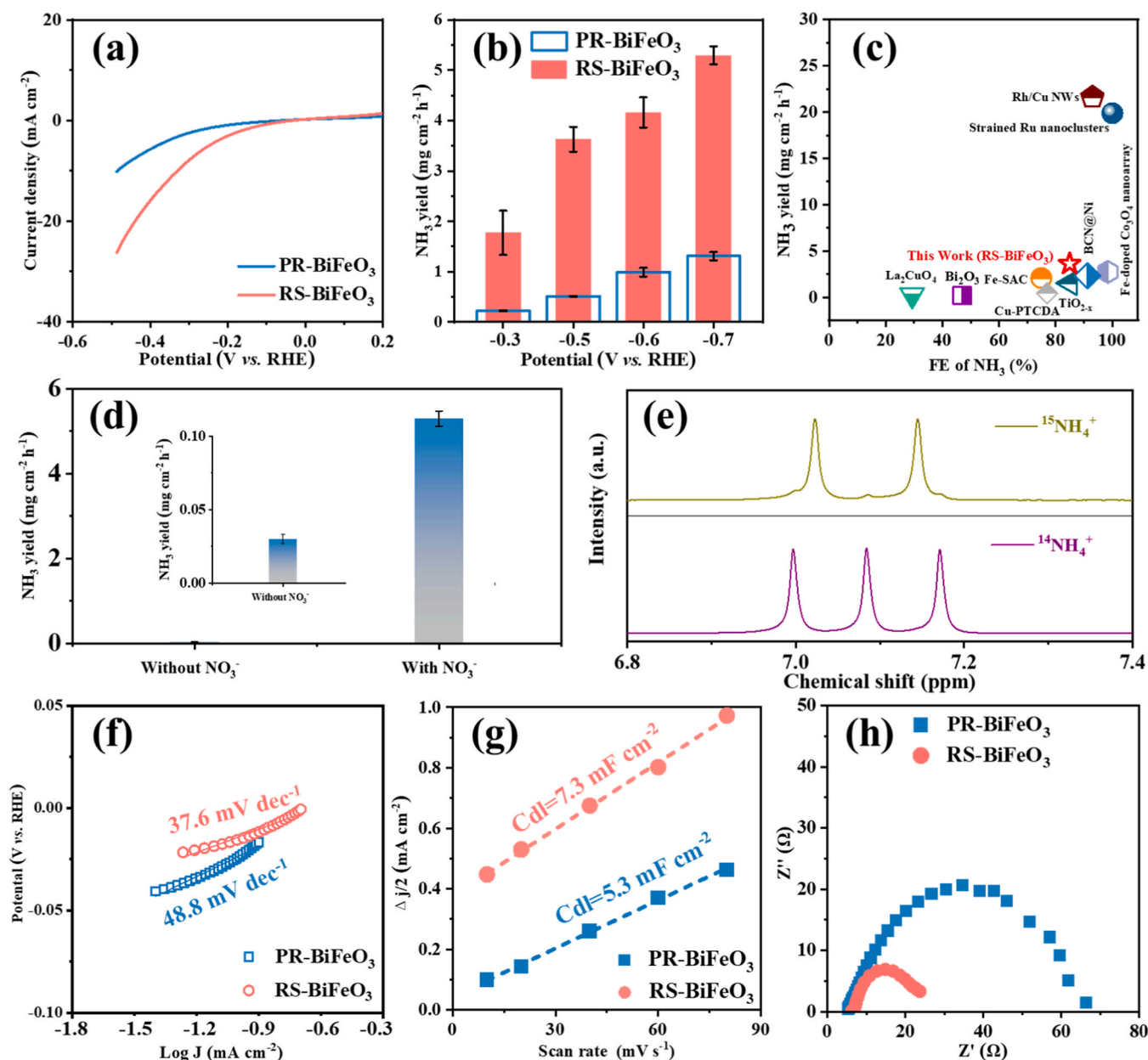


Fig. 2. (a) LSV curves. (b) NH₃ yield rate on PR-BiFeO₃ and RS-BiFeO₃ at different potentials. (c) The comparison of NO₃ catalytic activity with other electrocatalysts reported recently. (d) The NH₃ yield rate with and without NO₃ on RS-BiFeO₃ at potential of -0.7 V. (e) ¹H NMR measurement of the electrolyte with ¹⁵NO₃ and ¹⁴NO₃ as the N sources on RS-BiFeO₃. (f) The LSV-derived Tafel plots of PR-BiFeO₃ and RS-BiFeO₃. (g) Capacitive current density differences as a function of scan rate. (h) EIS curve.

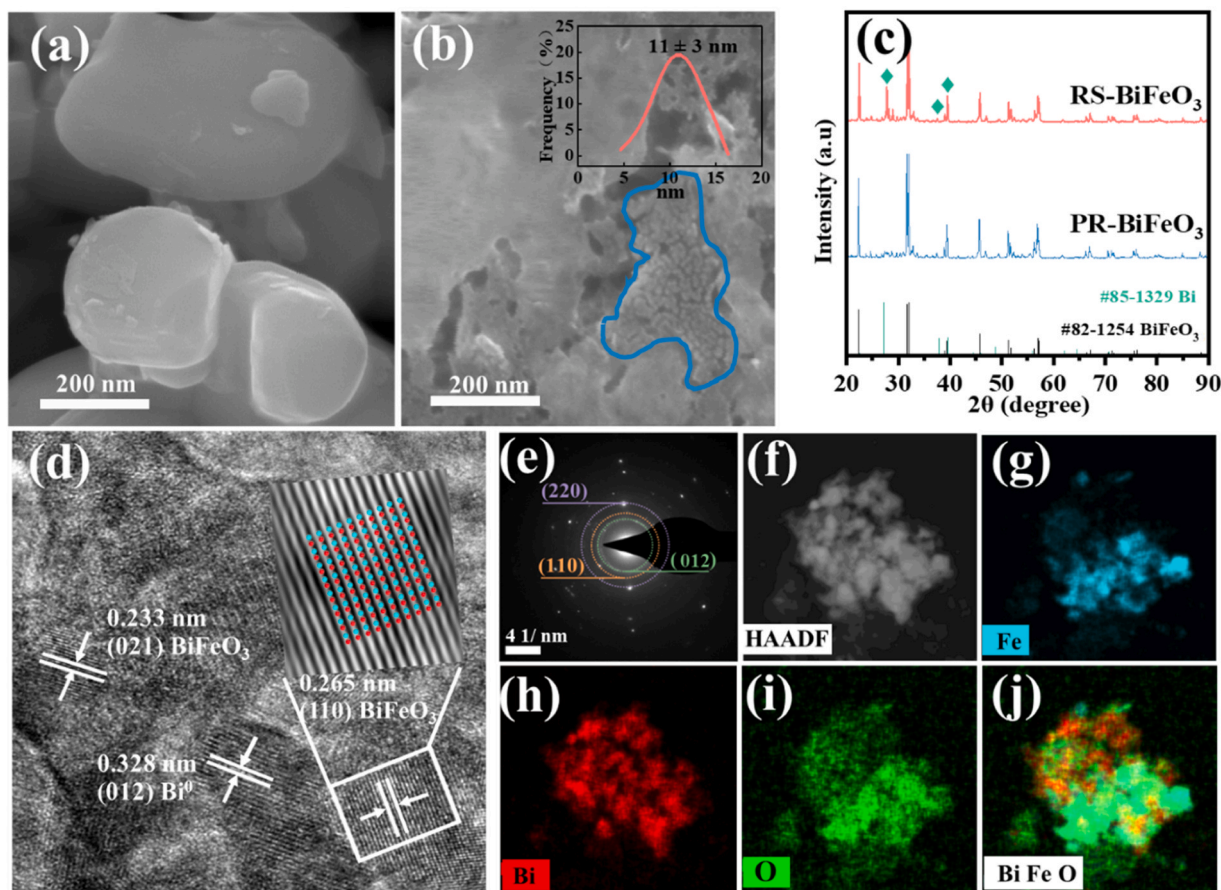


Fig. 3. BiFeO₃ surface characterizations. (a, b) SEM images and (c) XRD patterns for PR-BiFeO₃ and RS-BiFeO₃. (d) HR-TEM image of RS-BiFeO₃, (e) SAED pattern image and (f-i) TEM-EDS mapping for RS-BiFeO₃.

these results from the aforementioned electrochemical tests suggested the creation of additional active sites and achievement of faster interfacial electron transfer on the RS-BiFeO₃ electrode, culminating in improved NO₃RR catalytic activity.

3.2. Structural evolution of BiFeO₃ during NO₃RR

To uncover the surface reconstruction on BiFeO₃ during NO₃RR process, we performed physical characterization analysis on both PR-BiFeO₃ and RS-BiFeO₃. From the scan electron microscopy (SEM) images (Fig. 3a, b & Fig. S7), we observed significant changes on the BiFeO₃ catalyst surface. The PR-BiFeO₃ catalyst exhibited a granular morphology with dimensions of several hundred nanometers, while the RS-BiFeO₃ catalyst showcased irregular shaped structures. Notably, clusters with an estimated average size of 11 nm appeared on the surface of the RS-BiFeO₃ catalyst. XRD results presented in Fig. 3c revealed new diffraction peaks at 27.1°, 37.9° and 39.6° on the RS-BiFeO₃, compared to those of the PR-BiFeO₃ (JCPDS no. 82–1254). These peaks corresponded to the planes of metallic Bi (012), (104), and (110), respectively.

High resolution transmission electron microscope (HR-TEM) coupled with selected area electron diffraction (SAED) techniques were employed to further characterization of the morphology and crystalline structure of the RS-BiFeO₃. The HR-TEM images in Fig. 3d confirmed Bi⁰ exsolution from RS-BiFeO₃, with the observed lattice distance of 0.33 nm was corresponding to the (012) plane of Bi⁰ [37]. The SAED pattern in Fig. 3e illustrated the polycrystalline nature of the RS-BiFeO₃, with well-defined rings corresponding to the Bi⁰ (012), and BiFeO₃ (110) planes, respectively. Additionally, the high-angle annular dark field

(HAADF) image and energy dispersive spectroscopy (EDS) mappings (Fig. 3f-j) revealed an inhomogeneous distribution of elemental Bi, which can be attributed to the presence of Bi⁰ clusters. In comparison with the results of HR-TEM, SAED, and EDS for PR-BiFeO₃ in Fig. S8, these results clearly confirmed that the BiFeO₃ catalyst underwent surface reconstruction during the NO₃RR process, with a new phase, metallic Bi⁰ clusters, being in-situ formed.

X-ray photoelectron spectroscopy (XPS) analysis was performed on PR-BiFeO₃ and RS-BiFeO₃ that underwent 5, 10, 15 hours of cathodic polarization treatment, aiming to investigate their surface composition and chemical state (Fig. 4a-c, Fig. S9). The deconvoluted high-resolution Bi 4f XPS spectra of the samples are shown in Fig. 4a, revealing new peaks at 164.5 eV and 159.2 eV in the RS-BiFeO₃ catalyst compared to the PR-BiFeO₃, which can be attributed to metallic Bi⁰ [28, 38]. The process of Bi⁰ exsolution from BiFeO₃ during surface reconstruction might be described by the following Eqs. 1–3 [21,38]. In addition, the similar extents of Bi⁰ in RS-BiFeO₃ that underwent different cathodic polarization times demonstrated that the Bi⁰ generation from the interior of BiFeO₃ was limited, likely due to the kinetic barriers of Bi³⁺ transport through the BiFeO₃ lattice, similar to Sr³⁺ leaching from SrIrO₃ [39]. Interestingly, more oxygen vacancies (OVs) were observed in RS-BiFeO₃, as evidenced by a significant increase in the concentration of OVs from 23.2% for PR-BiFeO₃ to 41.0–47.5% for RS-BiFeO₃ (Fig. 4b and Table S2). A similar increasement trend in OVs content was observed, rising from 10.9% for PR-BiFeO₃ to 17.6% for RS-BiFeO₃, as determined by iodometry analysis. This finding also aligns with the EPR result (Fig. 4d, e). A slightly higher content of Fe²⁺ was obtained in the RS-BiFeO₃, which was related to partial reduction of Fe⁴⁺ and Fe³⁺ [40,41]. In addition, the impacts of cathodic potential and

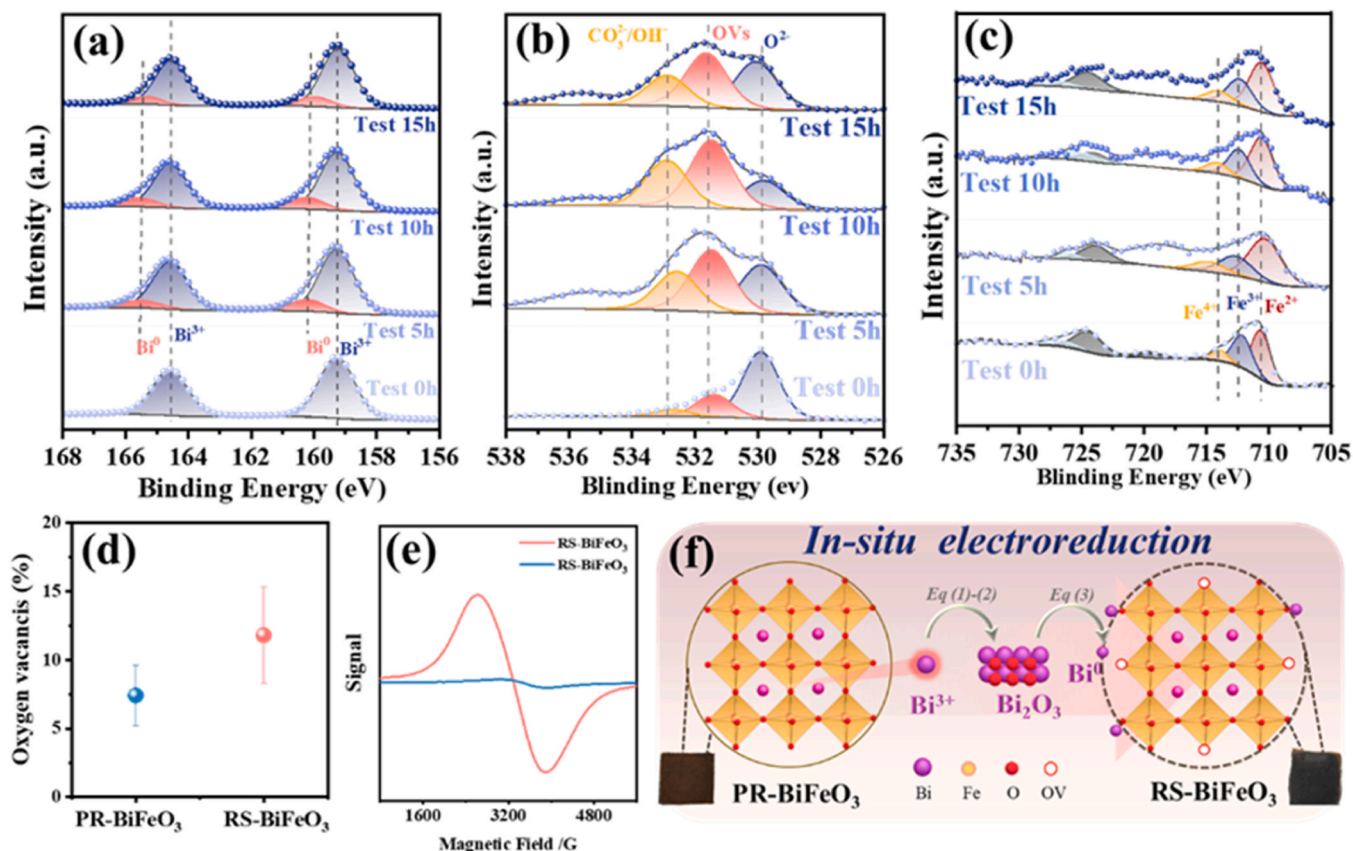


Fig. 4. (a-c) The corresponding deconvoluted XPS peaks of Bi4f, O1s and Fe2p spectra underwent different time treatment at -0.5 V vs. RHE. (d) Oxygen vacancies concentration obtained from iodometric titration. (e) EPR spectra of PR-BiFeO₃ and RS-BiFeO₃. (f) Schematic illustrations of BiFeO₃ evolution.

Cl⁻ on BiFeO₃ surface reconstruction were investigated. The results in Fig. S10 illustrated that at a cathodic polarization potential of -0.1 V, there was no observable evolution phenomenon, as the performance of NO₃RR showed no significant change, and no generation of Bi⁰, according to the results of SEM and XPS. However, when the cathodic polarization potential decreased to -0.3 V, the phenomenon of surface reconstruction occurs. Fig. S11 indicated that the presence of Cl⁻ had no discernible impact on BiFeO₃ surface reconstruction, as evidenced by the evolution of Bi⁰. A comparable extent of $\sim 14.0\%$ Bi⁰ was generated in RS-BiFeO₃ when polarized with or without Cl⁻ in the catholyte. To sum up, these characterization results suggest that the BiFeO₃ catalyst undergoes a significant structure evolution during the NO₃RR process. The formation of a new phase, Bi⁰, and the in-situ creation of numerous OVs in the surface of BiFeO₃ (Fig. 4e) could attribute to observed enhancement in catalytic activity for the reduction of NO₃ to NH₃.



3.3. Mechanistic insight into NO₃RR on BiFeO₃

To elucidate the profound role of OVs and Bi⁰, density functional theory (DFT) calculations were performed. Fig. S12 displays the atomistic structure model of PR-BiFeO₃ and RS-BiFeO₃ with Bi⁰ and OVs. Charge density differences (CDD) and bader charge analysis were conducted for NO₃ adsorption on the catalyst surfaces. As depicted in Fig. 5a, b, the bond length of the two N-O on PR-BiFeO₃ were 1.303 and 1.301 Å, respectively, which extended to 1.306 and 1.305 Å on RS-

BiFeO₃. The electrons transferred from PR-BiFeO₃ to adsorbed NO₃ (*NO₃) was 0.68 e⁻, lower than that of 0.75 e⁻ for RS-BiFeO₃. These results suggest enhanced activation of NO₃ on RS-BiFeO₃ compared to PR-BiFeO₃ [42,43]. Moreover, based on the NO₃ electroreduction pathway reported in previous studies, NO₃ is initially adsorbed onto the catalyst surface as *NO₃, which subsequently undergoes deoxygenation reaction to form *NO₂, *NO, and *N, followed by a hydrogenation process to successively form *NH, *NH₂, and *NH₃, successively [44,45]. The Gibbs free energy diagrams for adsorbed different N-intermediates along the above pathway on PR-BiFeO₃ and RS-BiFeO₃ were calculated and shown in Fig. S13 and Fig. 5c. An increase in adsorption energy for NO₃ on the RS-BiFeO₃ of -0.92 eV was observed compared to -0.41 eV on PR-BiFeO₃, indicating that RS-BiFeO₃ was preferable to NO₃ adsorption [46]. In the NO₃RR process, there are two conspicuous uphill steps, from *NO₂ to *NO and desorption of *NH₃. For the case of *NO₂ to *NO step, the potential barrier of PR-BiFeO₃ (0.31 eV) was significantly higher than that of 0.08 eV on RS-BiFeO₃, illustrating faster conversion of *NO₂ to *NO on RS-BiFeO₃. Although the desorption of NH₃ requires more energy on RS-BiFeO₃ than on PR-BiFeO₃ (0.69 vs. 0.36 eV), in an alkaline electrolyte, the product is likely to form ammonium (NH₄⁺) with a negligible desorption obstacle [42,47].

In addition, the relative energy for the dissociation of H₂O molecular to atomic hydrogen (*H, the Volmer step) on RS-BiFeO₃ was found to be -0.65 eV, implying that the Volmer reaction is thermodynamically favorable. In contrast, the formation of *H on PR-BiFeO₃ was markedly more challenging given that the Volmer reaction needs to overcome a relative energy as high as 0.97 eV (Fig. 5d). This evidence points to RS-BiFeO₃ favoring the formation of *H. Furthermore, the relative energy of H₂ evolution (the Heyrovsky step) was -0.47 eV on RS-BiFeO₃, which was more negative than that of PR-BiFeO₃ (0.18 eV) (Fig. 5e), signifying that RS-BiFeO₃ constrains the H₂ evolution. In summary, the DFT results

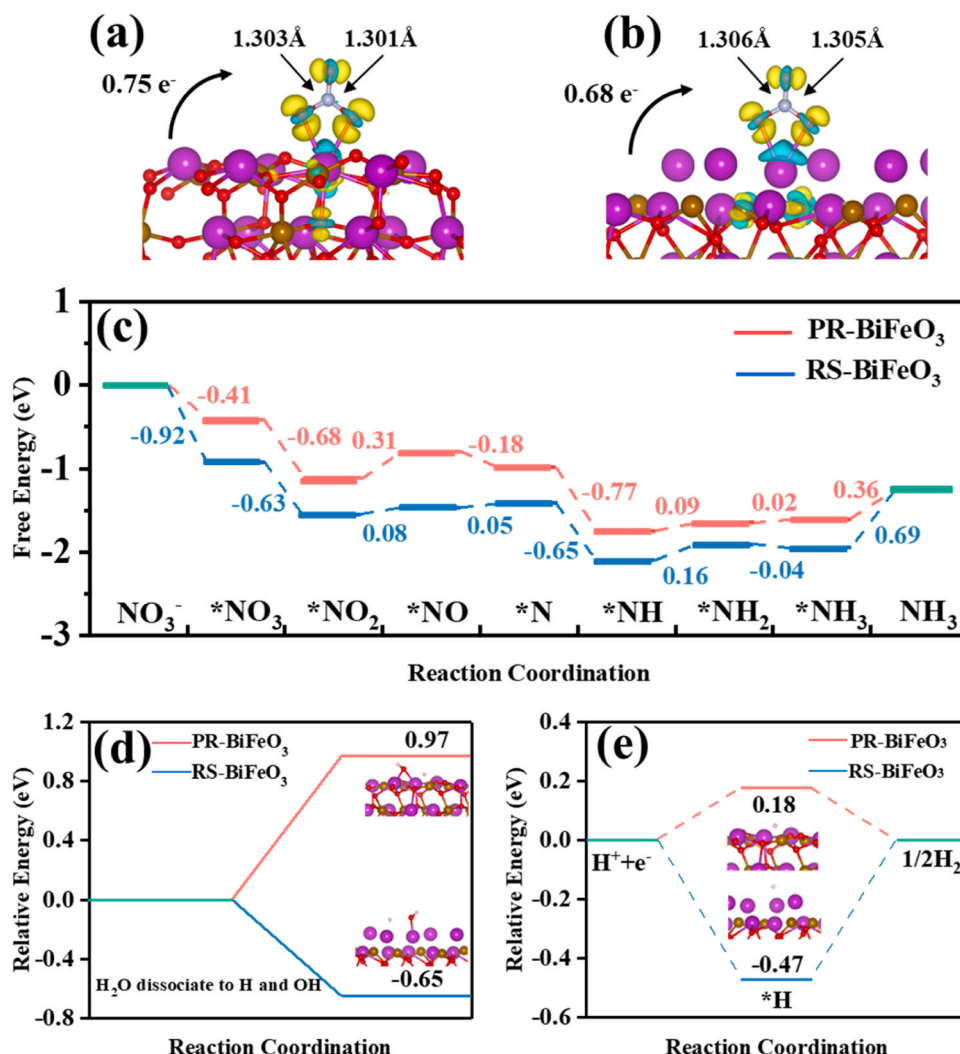


Fig. 5. Charge density difference plot of NO₃⁻ adsorbed on (a) PR-BiFeO₃ surface and (b) RS-BiFeO₃ surface. (c) NO₃RR Gibbs free energies diagrams of different N-intermediates on the PR-BiFeO₃ and RS-BiFeO₃ surface, respectively. (d) The relative energy for *H formation from H₂O dissociation and (e) the relative energy of H₂ evolution on the on PR-BiFeO₃ and RS-BiFeO₃ surface, respectively.

showed that RS-BiFeO₃, with exsolved Bi⁰ and an increased number of OV, can enhance NO₃ deoxidation by increasing NO₃ adsorption and accelerating the *NO₂ conversion to *NO. Additionally, RS-BiFeO₃ can simulate NO₃ hydrogenation by boosting *H generation and restricting H₂ formation, thereby notably promoting the selective electroreduction of NO₃ into NH₃.

To further verify the role of BiFeO₃ surface construction on NO₃ electroreduction, NO₃ degradation pathway was explored through experimental testing. Initially, the N-intermediates and products for NO₃-N electroreduction on RS-BiFeO₃ investigated through in situ differential electrochemical mass spectrometry (DEMS) [48]. The *m/z* signals of 17, 28, 30, and 44, corresponding to NH₃, N₂, NO, and N₂O respectively, appeared when the potential was adjusted from 0 to -1.6 V vs. SCE of LSV (Fig. 6a). The *m/z*=17 signal for NH₃ was the strongest, confirming the significant activity for NH₃ generation. Notably, a common intermediate, *NO₂, was not detected here, suggesting *NO₂ a swift conversion of *NO₂ to *NO [49]. Additionally, in comparison with PR-BiFeO₃, a lower NO₂-N accumulation rate (0.10 vs. 0.18 mg h⁻¹ cm⁻²) but a higher NO₃ removal rate (5.0 vs. 3.6 mg cm⁻² h⁻¹) were observed on the RS-BiFeO₃ (Fig. 6b). This evidence further affirms an ultrafast conversion of NO₂ to NO⁻ by RS-BiFeO₃, which is consistent with the DFT result, indicating that RS-BiFeO₃ can enhance NO₃ deoxidation by accelerating the conversion of *NO₂ to *NO.

Subsequently, whether NO₃ electroreduction proceeds via direct electron transfer (DET) or indirect *H reduction was determined. The role of *H was examined using EPR technique, where DMPO served as a radical trapping reagent. As depicted in Fig. 6c, the emergence of nine EPR peaks can be attributed to the DMPO-H signal [43], indicating the generation of atomic *H on the RS-BiFeO₃ surface. The introduction of NO₃ into the system caused a significant decline in DMPO-H peaks, suggesting *H consumption in NO₃ reduction. To confirm the contribution of the *H mediated pathway, tert-butyl alcohol (TBA) was utilized as a scavenger for *H (Fig. 6d) [31]. Observations revealed a decrease of 49.1% in the reaction rate constant (1.47 × 10⁻³ min⁻¹) with the addition of 15 mM TBA, compared to the reaction without TBA (2.89 × 10⁻³ min⁻¹). The aforementioned results underscore the essential role of *H in NO₃ electroreduction, which aligns with DFT calculations showing that *H facilitates NO₃ hydrogenation. Consequently, the NO₃ electroreduction pathway at RS-BiFeO₃ can be proposed as follows: Initially, NO₃ is adsorbed onto the active sites and subsequently reduced to NO_{3ad}. This is followed by the swift conversion of NO_{3ad} to NO_{2ad}. Partially, NO_{2ad} is selectively reduced to N₂O_{ad}, while a majority of NO_{2ad} is reduced by *H to NH₃ in stages, via intermediates such as N_{ad}, NH_{ad}, and NH_{2ad} (Eqs. S1–9).

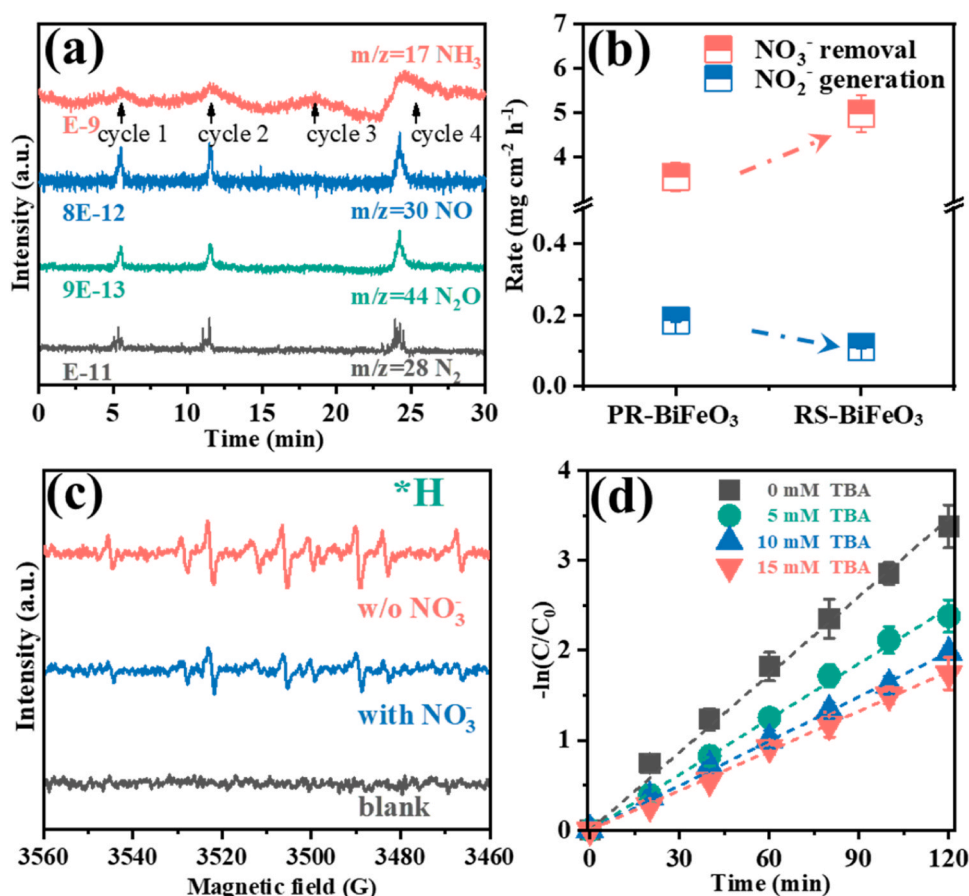


Fig. 6. (a) Mass spectrometry signals of in situ DEMS measurements (test potential from 0 to -1.6 V vs. SCE). (b) Reaction rates of NO_3^- removal and NO_2^- production on PR-BiFeO₃ and RS-BiFeO₃. (c) DMPO spin-trapping EPR spectra of RS-BiFeO₃ with or without NO_3^- -N. (d) The linearized pseudo first-order kinetic profiles of RS-BiFeO₃ with different addition concentration of TBA.

3.4. Stability of BiFeO₃ for nitrate wastewater treatment

The stability of BiFeO₃ was evaluated through the treatment of synthetic wastewater and real nitro cotton wastewater at continuous mode with a hydraulic retention time (HRT) of 24 h. During the initial 7 days, the continuous system treated synthetic nitrate-polluted wastewater with approximately $200 \text{ mg L}^{-1} \text{ NO}_3^-$ -N. Subsequently, real nitro cotton wastewater, featuring a comparable NO_3^- -N concentration, took the place of the synthetic wastewater for further treatment. The characteristics of the nitro cotton wastewater were described in Table S3. As depicted in Fig. 7, it was apparent that the effluent NO_3^- -N concentration from the synthetic wastewater was marginally lower than that of the nitro cotton wastewater, whereas the effluent NH_4^+ -N concentration was a bit higher than that of the nitro cotton wastewater. Consequently, the average NO_3^- -N removal efficiency and NH_4^+ -N selectivity for the synthetic wastewater were $71.0 \pm 3.8\%$ and $67.9 \pm 3.2\%$, respectively, compared to $61.0 \pm 3.8\%$ and $55.3 \pm 4.6\%$ for the real nitro cotton wastewater. The performance gap in NO_3^- RR between the synthetic and real wastewater may be attributed by the complex composition of the latter. Additionally, the calculated average FEs for the synthetic and nitro cotton wastewater were 15.5% and 11.0%, respectively. The relatively lower FEs observed in this study can be attributed to two factors: i) The lower NO_3^- -N concentration of approximately 60 mg L^{-1} resulted in a diminished FE. Previous studies have reported that a lower NO_3^- -N concentration typically leads to reduced FE [50,51]. For instance, LaFeO₃ exhibited an FE of only $\sim 8\%$ at an NO_3^- -N concentration of 50 mg L^{-1} (-0.6 V vs. RHE) [18]. ii) The utilization of a constant current mode of 15 mA cm^{-2} , corresponding to a very low potential of about -1.0 V vs. RHE, contributed to the decrease in FEs. When the

cathode potential was excessively low, a lower FE was obtained [52,53]. As an illustration, the FE decreased from $\sim 95\%$ at -0.3 V to $\sim 22\%$ at -0.5 V vs. RHE [54]. In general, the results obtained from Fig. 7 demonstrated the exceptional stability of BiFeO₃ for NO_3^- RR, indicating its significant potential for practical application.

4. Conclusions

An in-situ surface reconstruction of BiFeO₃ was observed, illustrated by an enhancement in NO_3^- RR that was correlated with reaction time. This process was further supported by the structural evolution of metallic Bi⁰ and the creation of oxygen vacancies (OVs). RS-BiFeO₃ demonstrated a significant improvement in NO_3^- RR compared to its pristine counterpart, as indicated by a series of electrochemical tests, such as LSV. Density functional theory (DFT) calculations revealed that the metallic Bi⁰ and OVs on RS-BiFeO₃ acted as the true active sites, facilitating both the deoxygenation and hydrogenation processes of the NO_3^- reaction, thereby augmenting catalytic activity. Furthermore, the NO_3^- reduction pathway was explored based on the results of online DEMS and a radical trapping test, confirming the crucial role of OVs and metallic Bi⁰. This study provides a comprehensive understanding of the BiFeO₃ catalyst's performance in NO_3^- reduction and broadens the application scope of ABO₃-type perovskite in NO_3^- RR.

CRediT authorship contribution statement

Shangtao Liang: Formal analysis. **Zejin Lin:** Resources, Methodology. **Jianxin Pan:** Validation, Resources. **Cao Yang:** Software, Investigation. **Tingting Zhu:** Validation, Investigation. **Sihao Lv:**

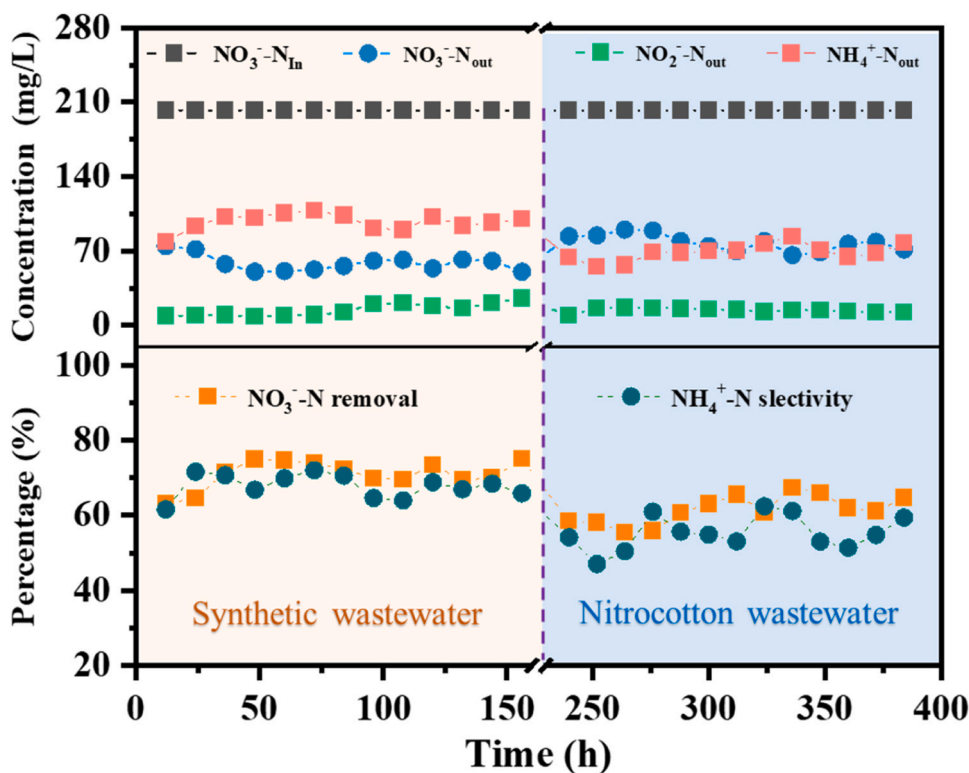


Fig. 7. Performance of synthetic and real nitrocotton wastewater treatment by reconstructed BiFeO₃ at continuous mode.

Resources, Project administration. **Hui Lin**: Visualization, Supervision. **Lihui Yang**: Writing – review & editing, Supervision, Project administration. **Wenjian Yang**: Data curation.

Declaration of Competing Interest

The authors declare that they have no known competing financial interests or personal relationships that could have appeared to influence the work reported in this paper.

Data Availability

Data will be made available on request.

Acknowledgments

This study was financially supported by the Basic and Applied Basic Research Foundation of Guangdong Province (2020A15110248), National Natural Science Foundation of China (No. 51878170, No. 52000027).

Appendix A. Supporting information

Supplementary data associated with this article can be found in the online version at doi:10.1016/j.apcatb.2024.123864.

References

- [1] Z.Y. Wu, M. Karamad, X. Yong, Q. Huang, D.A. Cullen, P. Zhu, C. Xia, Q. Xiao, M. Shakouri, F.Y. Chen, J.Y.T. Kim, Y. Xia, K. Heck, Y. Hu, M.S. Wong, Q. Li, I. Gates, S. Siahrostami, H. Wang, Electrochemical ammonia synthesis via nitrate reduction on Fe single atom catalyst, *Nature, Communications* 12 (2021) 2870.
- [2] S.I. Venturini, D.R. Martins de Godoi, J. Perez, Challenges in Electrocatalysis of ammonia oxidation on platinum surfaces: Discovering reaction pathways, *ACS, Catalysis* 13 (2023) 10835–10845.
- [3] Y. Liu, X. Kong, X. Guo, Q. Li, J. Ke, R. Wang, Q. Li, Z. Geng, J. Zeng, Enhanced N₂ electroreduction over LaCoO₃ by introducing oxygen vacancies, *ACS, Catalysis* 10 (2019) 1077–1085.
- [4] X. Li, P. Shen, X. Li, D. Ma, K. Chu, Sub-nm RuO_x clusters on Pd metallene for synergistically enhanced nitrate electroreduction to ammonia, *ACS Nano* 17 (2) (2023) 1081–1090.
- [5] Z. Wang, D. Richards, N. Singh, Recent discoveries in the reaction mechanism of heterogeneous electrocatalytic nitrate reduction, *Catal. Sci. Technol.* 11 (2021) 705–725.
- [6] G. Zhang, X. Li, K. Chen, Y. Guo, D. Ma, K. Chu, Tandem electrocatalytic nitrate reduction to ammonia on MBenes, *Angew. Chem. Int. Ed.* 62 (2023) e202300054.
- [7] X. Liu, J. Meng, J. Zhu, M. Huang, B. Wen, R. Guo, L. Mai, Comprehensive understandings into complete reconstruction of precatalysts: Synthesis, applications, and characterizations, *Adv. Mater.* 33 (2021) e2007344.
- [8] W. Duan, Y. Chen, H. Ma, J.F. Lee, Y.J. Lin, C. Feng, In situ reconstruction of metal oxide cathodes for ammonium generation from high-strength nitrate wastewater: elucidating the role of the substrate in the performance of Co₃O₄, *Environ. Sci. Technol.* 57 (2023) 3893–3904.
- [9] P. Shao, Z. Chang, M. Li, X. Lu, W. Jiang, K. Zhang, X. Luo, L. Yang, Mixed-valence molybdenum oxide as a recyclable sorbent for silver removal and recovery from wastewater, *Nat. Commun.* 14 (2023) 1365.
- [10] A. Zhang, Y. Liang, H. Li, B. Zhang, Z. Liu, Q. Chang, H. Zhang, C.F. Zhu, Z. Geng, W. Zhu, J. Zeng, In-situ surface reconstruction of InN nanosheets for efficient CO₂ electroreduction into formate, *Nano Lett.* 20 (2020) 8229–8235.
- [11] Y. Wang, W. Zhou, R. Jia, Y. Yu, B. Zhang, Unveiling the activity origin of a copper-based electrocatalyst for selective nitrate reduction to ammonia, *Angew. Chem. Int. Ed.* 59 (2020) 5350–5354.
- [12] J. Cai, S. Qin, M.A. Akram, X. Hou, P. Jin, F. Wang, B. Zhu, X. Li, L. Feng, In situ reconstruction enhanced dual-site catalysis towards nitrate electroreduction to ammonia, *J. Mater. Chem. A* 10 (2022) 12669–12678.
- [13] H. Jiang, Q. He, Y. Zhang, L. Song, Structural self-reconstruction of catalysts in electrocatalysis, *Acc. Chem. Res.* 51 (2018) 2968–2977.
- [14] H.Y. Wang, S.F. Hung, H.Y. Chen, T.S. Chan, H.M. Chen, B. Liu, In operando identification of geometrical-site-dependent water oxidation activity of spinel Co₃O₄, *J. Am. Chem. Soc.* 138 (2016) 36–39.
- [15] Y. Zeng, M. Zhao, Z. Huang, W. Zhu, J. Zheng, Q. Jiang, Z. Wang, H. Liang, Surface reconstruction of water splitting electrocatalysts, *Advanced Energy, Materials* 12 (2022) 2201713.
- [16] S. Li, Z. Li, R. Ma, C. Gao, L. Liu, L. Hu, J. Zhu, T. Sun, Y. Tang, D. Liu, J. Wang, A glass-ceramic with accelerated surface reconstruction toward the efficient oxygen evolution reaction, *Angew. Chem. Int. Ed.* 60 (2020) 3773–3780.
- [17] Y. Wang, L. Chen, H. Cao, Z. Chi, C. Chen, X. Duan, Y. Xie, F. Qi, W. Song, J. Liu, S. Wang, Role of oxygen vacancies and Mn sites in hierarchical Mn₂O₃/LaMnO_{3-δ} perovskite composites for aqueous organic pollutants decontamination, *Appl. Catal. B: Environ.* 245 (2019) 546–554.

- [18] K. Chu, W. Zong, G. Xue, H. Guo, J. Qin, H. Zhu, N. Zhang, Z. Tian, H. Dong, Y. E. Miao, M.B.J. Roeffaers, J. Hofkens, F. Lai, T. Liu, Cation substitution strategy for developing perovskite oxide with rich oxygen vacancy-mediated charge redistribution enables highly efficient nitrate electroreduction to ammonia, *J. Am. Chem. Soc.* 145 (2023) 21387–21396.
- [19] F. Liu, Z. Zhang, L. Shi, Y. Zhang, X. Qiu, Y. Dong, H. Jiang, Y. Zhu, J. Zhu, Promoting nitrate electroreduction to ammonia over A-site deficient cobalt-based perovskite oxides, *J. Mater. Chem. A* 11 (2023) 10596–10604.
- [20] J. Wang, D. Wu, M. Li, X. Wei, X. Yang, M. Shao, M. Gu, Bismuth ferrite as an electrocatalyst for the electrochemical nitrate reduction, *Nano Lett.* 22 (2022) 5600–5606.
- [21] C.-J. Ma, Y. Chen, C. Zhu, Q. Chen, W.-L. Song, S. Jiao, H. Chen, D. Fang, Bismuth ferrite: an abnormal perovskite with electrochemical extraction of ions from A site, *J. Mater. Chem. A* 7 (2019) 12176–12190.
- [22] K.H. Chung, H.H. Jung, S.J. Kim, Y.K. Park, S.C. Kim, S.C. Jung, Hydrogen production through catalytic water splitting using liquid-phase plasma over bismuth ferrite catalyst, *Int. J. Mol. Sci.* 22 (2021) 1–11.
- [23] C. Li, K. Li, C. Chen, Q.L. Tang, T.H. Sun, J.P. Jia, Electrochemical removal of nitrate using a nanosheet structured $\text{Co}_3\text{O}_4/\text{Ti}$ cathode: Effects of temperature, current and pH adjusting, *Sep. Purif. Technol.* 237 (2020) 116485.
- [24] S. Grimme, J. Antony, S. Ehrlich, H. Krieg, A consistent and accurate ab initio parametrization of density functional dispersion correction (DFT-D) for the 94 elements H-Pu, *The. J. Chem. Phys.* 132 (2010) 154104.
- [25] M.H. J, P.J. D, Special points for Brillouin-zone integrations, *Phys. Rev. B* 13 (2022) 5188.
- [26] L. Chen, Y. Zhang, C. Ma, Perovskites $\text{Sr}_{1-x}\text{La}_x\text{Mn}_y\text{Co}_{1-y}\text{O}_{3-\delta}$ coated on Ti as stable non-noble anode for efficient electrocatalytic oxidation of organic wastewater containing ammonia nitrogen, *Chem. Eng. J.* 393 (2020) 124514.
- [27] J. Sun, W. Gao, H. Fei, G. Zhao, Efficient and selective electrochemical reduction of nitrate to N_2 by relay catalytic effects of Fe-Ni bimetallic sites on MOF-derived structure, *Appl. Catal. B: Environ.* 301 (2022) 120829.
- [28] M. Chen, J. Bi, X. Huang, T. Wang, Z. Wang, H. Hao, Bi_2O_3 nanosheets arrays in-situ decorated on carbon cloth for efficient electrochemical reduction of nitrate, *Chemosphere* 278 (2021) 130386.
- [29] J. Li, G. Zhan, J. Yang, F. Quan, C. Mao, Y. Liu, B. Wang, F. Lei, L. Li, A.W.M. Chan, L. Xu, Y. Shi, Y. Du, W. Hao, P.K. Wong, J. Wang, S.X. Dou, L. Zhang, J.C. Yu, Efficient ammonia electrosynthesis from nitrate on strained ruthenium nanoclusters, *J. Am. Chem. Soc.* 142 (2020) 7036–7046.
- [30] P. Wei, J. Liang, Q. Liu, L. Xie, X. Tong, Y. Ren, T. Li, Y. Luo, N. Li, B. Tang, A. M. Asiri, M.S. Hamdy, Q. Kong, Z. Wang, X. Sun, Iron-doped cobalt oxide nanoarray for efficient electrocatalytic nitrate-to-ammonia conversion, *J. Colloid Interface Sci.* 615 (2022) 636–642.
- [31] W.-J. Yang, L.-H. Yang, H.-J. Peng, S.-H. Lv, H. Muhammad Adeel Sharif, W. Sun, W. Li, C. Yang, H. Lin, Perovskite oxide $\text{LaMO}_{3-\delta}$ ($M = \text{Fe}, \text{Co}, \text{Ni}$ and Cu) cathode for efficient electroreduction of nitrate, *Sep. Purif. Technol.* 295 (2022) 121278.
- [32] G.-F. Chen, Y. Yuan, H. Jiang, S.-Y. Ren, L.-X. Ding, L. Ma, T. Wu, J. Lu, H. Wang, Electrochemical reduction of nitrate to ammonia via direct eight-electron transfer using a copper-molecular solid catalyst, *Nat. Energy* 5 (2020) 605–613.
- [33] R. Jia, Y. Wang, C. Wang, Y. Ling, Y. Yu, B. Zhang, Boosting selective nitrate electroreduction to ammonium by constructing oxygen vacancies in TiO_2 , *ACS Catal.* 10 (2020) 3533–3540.
- [34] X. Zhao, Z. Zhu, Y. He, H. Zhang, X. Zhou, W. Hu, M. Li, S. Zhang, Y. Dong, X. Hu, A.V. Kuklin, G.V. Baryshnikov, H. Ågren, T. Wågberg, G. Hu, Simultaneous anchoring of Ni nanoparticles and single-atom Ni on BCN matrix promotes efficient conversion of nitrate in water into high-value-added ammonia, *Chem. Eng. J.* 433 (2022) 133190.
- [35] H. Liu, X. Lang, C. Zhu, J. Timoshenko, M. Ruscher, L. Bai, N. Guijarro, H. Yin, Y. Peng, J. Li, Z. Liu, W. Wang, B.R. Cuenya, J. Luo, Efficient electrochemical nitrate reduction to ammonia with copper-supported rhodium cluster and single-atom catalysts, *Angew. Chem. Int. Ed.* 61 (2022) e202202556.
- [36] R. Zhao, Q. Yan, L. Yu, T. Yan, X. Zhu, Z. Zhao, L. Liu, J. Xi, A. Bi-Co, corridor construction effectively improving the selectivity of electrocatalytic nitrate reduction toward ammonia by nearly 100, *Adv. Mater.* 35 (2023) e2306633.
- [37] W. He, Y. Sun, G. Jiang, H. Huang, X. Zhang, F. Dong, Activation of amorphous Bi_2WO_6 with synchronous Bi metal and Bi_2O_3 coupling: photocatalysis mechanism and reaction pathway, *Appl. Catal. B: Environ.* 232 (2018) 340–347.
- [38] E. Zhang, T. Wang, K. Yu, J. Liu, W. Chen, A. Li, H. Rong, R. Lin, S. Ji, X. Zheng, Y. Wang, L. Zheng, C. Chen, D. Wang, J. Zhang, Y. Li, Bismuth single atoms resulting from transformation of metal-organic frameworks and their use as electrocatalysts for CO_2 reduction, *J. Am. Chem. Soc.* 141 (2019) 16569–16573.
- [39] Linsey C. Seitz, K.N. Colin, F. Dickens, Yasuyuki Hikita, A.D. Joseph Montoya, A.V. Charlotte Kirk, J.K.N. Harold Y. Hwang, Thomas F. Jaramillo, A highly active and stable $\text{IrOx}/\text{SrIrO}_3$ catalyst for the oxygen evolution reaction, *Science* 353 (2016) 1011–1014.
- [40] Y. Bu, Q. Zhong, D. Xu, W. Tan, Redox stability and sulfur resistance of $\text{Sm}_{0.9}\text{Sr}_{0.1}\text{Cr}_x\text{Fe}_{1-x}\text{O}_{3-\delta}$ perovskite materials, *J. Alloy. Compd.* 578 (2013) 60–66.
- [41] X. Tian, C. Zheng, H. Zhao, Ce-modified $\text{SrFeO}_{3-\delta}$ for ethane oxidative dehydrogenation coupled with CO_2 splitting via a chemical looping scheme, *Appl. Catal. B: Environ.* 303 (2022) 120894.
- [42] K. Wu, C. Sun, Z. Wang, Q. Song, X. Bai, X. Yu, Q. Li, Z. Wang, H. Zhang, J. Zhang, X. Tong, Y. Liang, A. Khosla, Z. Zhao, Surface reconstruction on uniform Cu nanodisks boosted electrochemical nitrate reduction to ammonia, *ACS Mater. Lett.* 4 (2022) 650–656.
- [43] Y. Zhang, X. Chen, W. Wang, L. Yin, J.C. Crittenden, Electrocatalytic nitrate reduction to ammonia on defective $\text{Au}/\text{Cu}(111)$ single-atom alloys, *Appl. Catal. B: Environ.* 310 (2022) 121346.
- [44] Y. Zhang, H. Zheng, K. Zhou, J. Ye, K. Chu, Z. Zhou, L. Zhang, T. Liu, Conjugated coordination polymer as a new platform for efficient and selective electroreduction of nitrate into ammonia, *Adv. Mater.* 35 (2023) e2209855.
- [45] L.-H. Yang, Z.-Q. Lin, M.-T. Liao, W.-J. Yang, J.-X. Pan, W. Li, C. Yang, Y.-J. Wu, G.-Z. Wang, S.-H. Lv, Engineering oxygen vacancies in perovskite oxides by in-situ electrochemical activation for highly efficient nitrate reduction, *Appl. Surf. Sci.* 639 (2023) 158208.
- [46] X. Chen, T. Zhang, M. Kan, D. Song, J. Jia, Y. Zhao, X. Qian, Binderless and oxygen vacancies rich $\text{FeNi}/\text{graphitized mesoporous carbon}/\text{Ni}$ foam for electrocatalytic reduction of nitrate, *Environ. Sci. Technol.* 54 (2020) 13344–13353.
- [47] Z. Wang, C. Sun, X. Bai, Z. Wang, X. Yu, X. Tong, Z. Wang, H. Zhang, H. Pang, L. Zhou, W. Wu, Y. Liang, A. Khosla, Z. Zhao, Facile synthesis of carbon nanobelts decorated with Cu and Pd for nitrate electroreduction to ammonia, *ACS Appl. Mater. Interfaces* 14 (2022) 30969–30978.
- [48] Y. Wang, C. Wang, M. Li, Y. Yu, B. Zhang, Nitrate electroreduction: mechanism insight, in situ characterization, performance evaluation, and challenges, *Chem. Soc. Rev.* 50 (2021) 6720–6733.
- [49] B. Xu, Z. Chen, G. Zhang, Y. Wang, On-demand atomic hydrogen provision by exposing electron-rich cobalt sites in an open-framework structure toward superior electrocatalytic nitrate conversion to dinitrogen, *Environ. Sci. Technol.* 56 (2021) 614–623.
- [50] Y. Ren, F. Tian, L. Jin, Y. Wang, J. Yang, S. You, Y. Liu, Fluidic MXene electrode functionalized with iron single atoms for selective electrocatalytic nitrate transformation to ammonia, *Environ. Sci. Technol.* 57 (2023) 10458–10466.
- [51] Y. Xue, Q. Yu, Q. Ma, Y. Chen, C. Zhang, W. Teng, J. Fan, W.X. Zhang, Electrocatalytic hydrogenation boosts reduction of nitrate to ammonia over single-atom Cu with $\text{Cu}(\text{I})\text{-N}(3)\text{C}(1)$ Sites, *Environ. Sci. Technol.* 56 (2022) 14797–14807.
- [52] J. Zhou, M. Wen, R. Huang, Q. Wu, Y. Luo, Y. Tian, G. Wei, Y. Fu, Regulating active hydrogen adsorbed on grain boundary defects of nano-nickel for boosting ammonia electrosynthesis from nitrate, *Energy Environ. Sci.* 16 (2023) 2611–2620.
- [53] X. Tong, Z. Zhang, Z. Fang, J. Guo, Y. Zheng, X. Liang, R. Liu, L. Zhang, W. Chen, PdMoCu Trimetalenes for Nitrate Electroreduction to Ammonia, *The. J. Phys. Chem. C* 127 (2023) 5262–5270.
- [54] J. Wang, C. Cai, Y. Wang, X. Yang, D. Wu, Y. Zhu, M. Li, M. Gu, M. Shao, Electrocatalytic reduction of nitrate to ammonia on low-cost ultrathin CoOx nanosheets, *ACS, Catalysis* 11 (2021) 15135–15140.